# Effective properties of acoustic metamaterial chains with low-frequency bandgaps controlled by the geometry of lightweight attachments

Luke G. Bennetts[1], Malte. A. Peter[2,3], Paul Dylejko[4], Alex Skvortsov[4]

[1]School of Mathematical Sciences, University of Adelaide, Adelaide, SA 5005, Australia

[2]Institute of Mathematics, University of Augsburg, 86135 Augsburg, Germany

[3] Augsburg Centre for Innovative Technologies, University of Augsburg, 86135 Augsburg Germany

[4] Maritime Division, Defense Science and Technology, Melbourne, VIC 3207, Australia

**Abstract**

The effective mass of an acoustical metamaterial chain, which consists of a modified monatomic chain with a lightweight attached mass–link system, is derived and used to analyse its low-frequency vibration-isolation properties. The effective mass is expressed in terms of the resonant and anti-resonant frequencies of a basic element of the chain, and it is shown that the geometry of the attached system can be used to lower the resonant and anti-resonant frequencies, in turn lowering the bandgap of the chain, and producing efficient low-frequency vibration isolation with lightweight attached masses. In certain parameter limits, the chain is shown to degenerate to two previously proposed chains with contrasting band structures, and this provides insights into controlling the underlying vibration-isolation mechanisms. Numerical simulations are presented that illustrate the efficiency of the proposed system in terms of minimising transmission of a low-frequency incident wave packet with only two units of the attached system.



## 1 Introduction

Developing systems to isolate low-frequency structural vibrations, i.e. the components that propagate long distances without inherent structural damping, has applications to microscopy [1], aerospace [2], health monitoring [3], and shipping [4], among many others. The field of acoustic metamaterials provides a general framework to achieve low-frequency vibration isolation, where the term metamaterial generally refers to systems incorporating resonant sub-wavelength elements that create unnatural effective properties, such as negative material constants, in frequency ranges around the resonances, which prohibit propagation of vibrations. Reviews are given by Ma et al. [5] and Chen et al. [6], and in the book by Craster & Guenneau [7]. The field has progressed to theoretical, numerical and experimental realisations of broadband low-frequency vibration isolation, e.g. for plates with cavities [8] or attached pillars [9, 10] or a combination of cavities and pillars [11, 12], and porous structures that simultaneously isolate both acoustic and elastic vibrations [13].

A canonical setting in the context of developing acoustic metamaterials for vibration isolation is an infinite monatomic chain, consisting of masses $m$ and springs $k$, to which a system is attached. In the absence of an attached system, longitudinal vibrations propagate along the chain for angular frequencies $\omega$ satisfying $m < 4\,k\,/\,\omega^2$, i.e. low-frequency waves propagate along the chain. In comparison, high-frequency vibrations, for which $m > 4\,k\,/\,\omega^2$, attenuate with distance along the chain, although high-frequency attenuation is not of interest in the present study. A standard metamaterial approach is to attach a mass $M$ to each mass $m$ with a (massless) spring $K$ [e.g. 14], as shown in Fig. 1(a). This is commonly known as the mass-in-mass system/chain, and has been generalised to systems with multiple degrees of freedom [e.g. 15] and involving nonlinearity [e.g. 16].

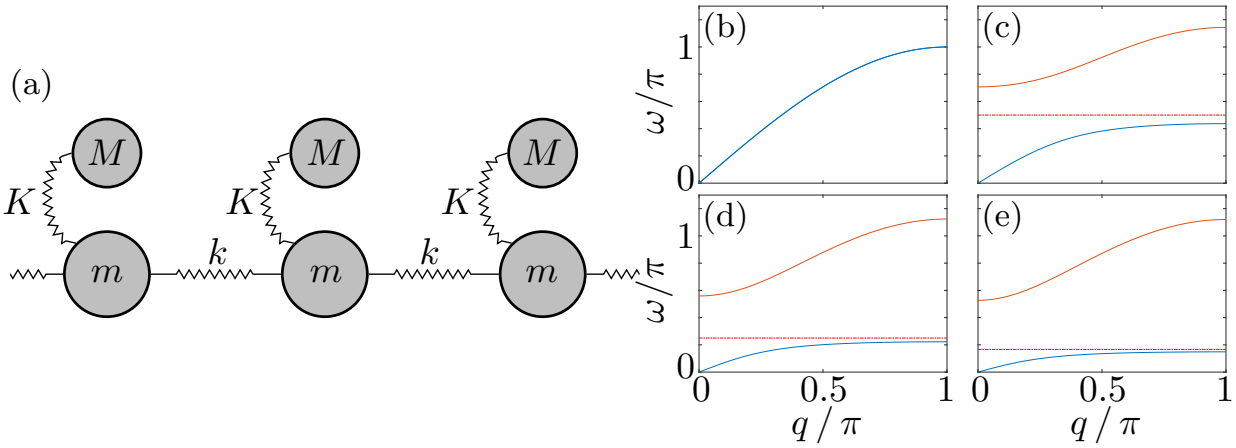


Figure 1: (a) Schematic of the mass-in-mass chain. (b–e) Corresponding band diagrams showing the acoustical (—) and optical (—) branches, for $m = 1$, $k = K = \pi^2 / 4$ and (b) $M = 0$, (c) $M = m$, (d) $M = 4\,m$, (d) $M = 9\,m$. Anti-resonant frequencies $\omega_* = \sqrt{M / K}$ are overlaid (···).

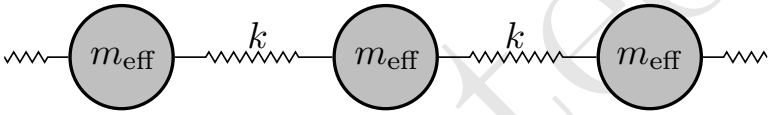


Figure 2: Schematic of the effective monatomic chain.

The attached system creates a local resonance, $\omega = \omega_*$, which is referred to here as an anti-resonance (for reasons that will become clear in § 2), and a surrounding frequency interval in which vibrations attenuate along the chain without the presence of a dissipative mechanism. For the mass-in-mass system, the anti-resonant frequency is $\omega_* = \sqrt{K / M}$, meaning arbitrarily low anti-resonances can be attained by increasing the attached mass, resulting in low-frequency vibration isolation. This process is illustrated by the band diagrams shown in Figs. 1(b–e), i.e. dispersion curves $\omega(q)$, where $q \in [0, \pi]$ is the wavenumber (defined in § 2.2), with the anti-resonant frequencies overlaid (···). Fig. 1(b) shows the band diagram for the monatomic chain (no attached mass, $M = 0$), for which the anti-resonant frequency does not exist; there is a single band (dispersion curve) for frequencies $\omega$ such that

$$0 < \omega < 2\sqrt{\frac{k}{m}} = \pi \quad \text{as} \quad k = \frac{\pi^2}{4} \quad \text{and} \quad m = 1, \tag{1}$$

which is known as an acoustical branch, and defines frequencies at which vibrations propagate along the chain. Figs. 1(c–e) show band diagrams for mass-in-mass chains ($M \neq 0$), with (c) $M = m$, (d) $M = 4\,m$, and (e) $M = 9\,m$. In these cases, there are two bands: an acoustical branch (—) at lower frequencies, and a curve occupying a higher-frequency interval known as the optical branch (—). The branches are separated by a frequency interval known as a bandgap, which defines relatively low-frequency ranges for which vibrations attenuate along the chain. The bandgap contains the anti-resonant frequency, with vibrations at surrounding frequencies strongly attenuated, i.e. efficient vibration isolation. As the attached mass is increased, the acoustical branch, anti-resonant frequency and bandgap all shift to lower frequencies, resulting in low-frequency vibration isolation.

Calculating the so-called effective properties of the mass-in-mass chain provides insights into the band structures shown in Figs. 1(b–e), and hence methods to control the vibration-isolation properties

of the system. For instance, the mass-in-mass chain can be mapped to the monatomic chain shown in Fig. 2, with springs $k$ and effective, frequency-dependent masses [see 14, Eq. 2]

$$m_{\text{eff}}(\omega) = m + \frac{M\,\omega_*^2}{\omega_*^2 - \omega^2}. \tag{2}$$

Therefore, the effective mass is unbounded as $\omega \to \omega_*$.The effective mass is positive in the limit from below, meaning the narrow bandgap intervals below the anti-resonant frequencies are associated to the inequality $m_{\text{eff}} > 4\,k\,/\,\omega^2$. In contrast, the effective mass is negative in the limit from above, so that the wider bandgap intervals above the anti-resonant frequencies are associated with $m_{\text{eff}} < 0$.

In practice, the attached mass is likely to be restricted by design considerations, thus limiting the lowest frequency at which vibration isolation can be achieved. An attractive alternative is to attach a lightweight system with geometry that provides control of the anti-resonant frequency, rather than using the attached mass to control the anti-resonant frequency. Fig. 3 shows a schematic of the chain to be studied, which consists of a modified monatomic chain, with masses $m$ and alternating springs $k$ and $K$, and lightweight masses $M$ above and below the $K$-springs that are attached to the masses either side of the $K$-springs with rigid, massless links. In a seminal study, Yilmaz et al. [17] considered a similar attached mass–link system, and showed that it produces low-frequency bandgaps when applied to a two-dimensional mass–spring lattice. Yilmaz & Hulbert [18] backed the finding with numerical simulations for finite lattices, and Acar & Yilmaz [19] showed that a similar approach can be used for one- and two-dimensional distributed parameter systems. Huang & Sun [20] studied a cognate mass–link system attached to a monatomic chain, where, motivated by possible practical material designs, the mass is connected to the links by a spring. They showed that the bandgaps produced by the system are associated with an elastic continuum (rather than an effective chain) with a negative effective Young's modulus, and illustrated the vibration-isolation properties with numerical simulations, in which 12 units of the system are applied in the middle of a monatomic chain to minimise transmission of an incident wave packet. Following the work of Yilmaz and co-workers, Frandsen et al. [21] proposed a mass–link system arranged periodically along an elastic rod, and showed numerically that the system isolates low-frequency longitudinal vibrations.

Bobrovnitskii [22] studied a similar chain to the one shown in Fig. 3 theoretically, but in which the masses $m = 0$, and the springs $K$ are absent, i.e. it cannot be considered in the context set out above of a monatomic chain with attachments (thus motivating our consideration of a modified monatomic chain). He found that the band structure involves an optical branch above a gap that stretches to zero frequency, and showed that low frequencies are associated with negative effective material properties. Oh et al. [23] also achieved zero-frequency bandgaps, both numerically and experimentally along a diatomic chain with spin applied to the smaller masses via link mechanisms to generate zero effective stiffness, in a broadly analogous fashion to [24]. Foehr et al. [25] recently showed how annular spiral-shaped voids in an elastic body can be used to generate inertial-amplification-type behaviour and produce wide low-frequency bandgaps.

In this work, the chain shown in Fig. 3 is used to generalise (i) a monatomic chain with the attached system proposed by Yilmaz and co-workers, and (ii) the chain proposed by Bobrovnitskii. The vibration-isolation properties of the chain are analysed in terms of the resonant and anti-resonant frequencies of a basic element, and a compact, general method is developed to calculate the effective mass of the chain. The effective mass is expressed in terms of the resonant and anti-resonant frequencies, and this empowers control over the band structure using the geometry of the attached system, particularly with respect to lowering its acoustical branch and moving the anti-resonant frequency into the bandgap between the acoustical and optical branches, thereby achieving efficient low-frequency vibration isolation. It is shown that the Yilmaz et al. and Bobrovnitskii chains can be recovered in certain parameter limits, thus revealing how the band structure of the proposed chain transitions from an isolated low-frequency acoustical branch (Yilmaz et al. chain) to an isolated optical branch above a gap stretching to zero frequency (Bobrovnitskii chain). The low-frequency vibration-isolation

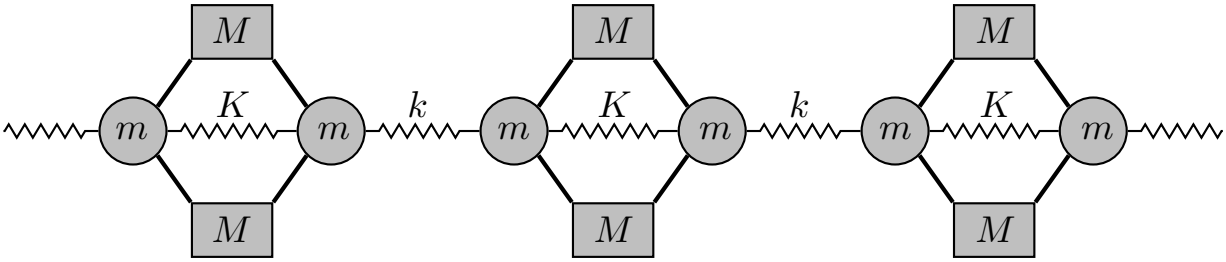


Figure 3: Schematic of the chain to be studied, involving lightweight attached masses $M$ and rigid massless links (—).

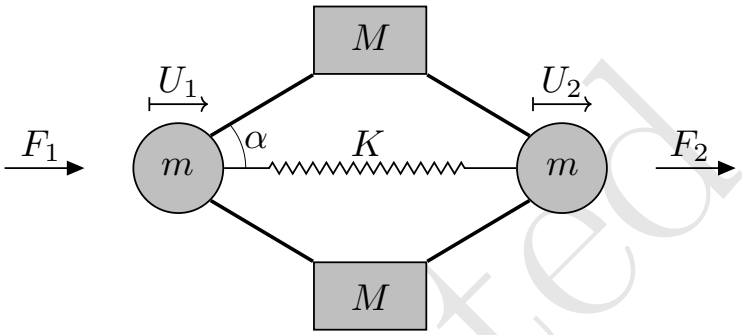


Figure 4: Schematic of a basic element of the chain shown in Fig. 3, with applied forces $F_j(t)$ and resulting displacements $U_j(t)$ $(j = 1, 2)$.

properties of the proposed system are illustrated via numerical simulations, in the vein of [20], but in which only two units of the system are attached in the middle of a monatomic chain, and the geometry is tuned to minimise transmission of an incident wave packet.



## 2 Equations of motion

### 2.1 Basic element: Resonant and anti-resonant frequencies

Consider the basic element shown in Fig. 4, consisting of a horizontal spring $K$ connecting two identical masses $m$, to which two additional masses $M$ are attached above and below by rigid links, where the links make an angle $\alpha$ with the horizontal. Horizontal forces $F_1(t)$ and $F_2(t)$ are applied to the left- and right-hand masses $m$, respectively, and the resulting horizontal displacements of the masses $m$ are denoted $U_1(t)$ and $U_2(t)$, respectively. The linearised equations of motion are

$$F_1 = \left(m + \frac{1}{2}\,M\,(1+\gamma^2)\right)\,\frac{\mathrm{d}^2U_1}{\mathrm{d}t^2} + \frac{1}{2}\,M\,(1-\gamma^2)\,\frac{\mathrm{d}^2U_2}{\mathrm{d}t^2} + K\,(U_1 - U_2) \tag{3a}$$

$$\text{and} \quad F_2 = \frac{1}{2}\,M\,(1-\gamma^2)\,\frac{\mathrm{d}^2U_1}{\mathrm{d}t^2} + \left(m + \frac{1}{2}\,M\,(1+\gamma^2)\right)\,\frac{\mathrm{d}^2U_2}{\mathrm{d}t^2} + K\,(U_2 - U_1), \tag{3b}$$

where $t$ is time and $\gamma = \cot\alpha$ is a geometrical parameter. For time-harmonic motions of the form

$$U_j(t) = u_j\,\mathrm{e}^{-\mathrm{i}\omega t} \quad \text{and} \quad F_j(t) = f_j\,\mathrm{e}^{-\mathrm{i}\omega t} \quad \text{for} \quad j = 1, 2, \tag{4}$$

the matrix/vector form of Eqs. (3) is

$$\begin{pmatrix} f_1 \\ f_2 \end{pmatrix} = \mathbf{C}_0 \begin{pmatrix} u_1 \\ u_2 \end{pmatrix} \quad \text{where} \quad \mathbf{C}_0 = \begin{pmatrix} \hat{c}_1 & \hat{c}_2 \\ \hat{c}_2 & \hat{c}_1 \end{pmatrix} \tag{5}$$

is the (dynamic) stiffness matrix, with entries

$$\hat{c}_1(\omega) = K - \omega^2 \left( m + \frac{1}{2} M \left(1 + \gamma^2\right) \right) \quad \text{and} \quad \hat{c}_2(\omega) = -K - \frac{1}{2} \omega^2 M \left(1 - \gamma^2\right). \tag{6}$$

The reciprocal relationship is

$$\begin{pmatrix} u_1 \\ u_2 \end{pmatrix} = \mathbf{D}_0 \begin{pmatrix} f_1 \\ f_2 \end{pmatrix} \quad \text{where} \quad \mathbf{D}_0 = \text{inv}\{\mathbf{C}_0\} = \begin{pmatrix} \hat{d}_1 & \hat{d}_2 \\ \hat{d}_2 & \hat{d}_1 \end{pmatrix} \tag{7}$$

is the (dynamic) compliance matrix, with entries $\hat{d}_1 = \Delta\, \hat{c}_1$ and $\hat{d}_2 = -\Delta\, \hat{c}_2$, in which

$$\Delta^{-1} = \det\{C_0\} = \omega^4 \left\{ m^2 + m\, M \left(1 + \gamma^2\right) + M^2\, \gamma^2 \right\} - 2\, \omega^2\, K\, m\, M. \tag{8}$$

The resonant frequency of the basic element is $\omega = \omega_0$, where

$$\omega_0 = \sqrt{\frac{2\, K}{m + M\, \gamma^2}} \quad \text{is defined by} \quad \det\{\mathbf{C}_0(\omega_0)\} = 0, \tag{9}$$

i.e. the compliance matrix $\mathbf{D}_0(\omega_0)$ is undefined at the resonant frequency. The anti-resonant frequency is $\omega = \omega_*$, where

$$\omega_* = \sqrt{\frac{2\, K}{M \left(\gamma^2 - 1\right)}} \in \mathbb{R} \quad \text{for} \quad \gamma > 1, \tag{10}$$

so that the anti-resonant frequency exists for angles $\alpha < \pi\,/\,4$ only. At the anti-resonant frequency $\hat{c}_2 = \hat{d}_2 = 0$, meaning energy cannot be transferred across the basic element. The resonant and anti-resonant frequencies can be made arbitrarily small by increasing the attached mass $M$ (similarly to the mass-in-mass chain) or increasing the geometrical parameter $\gamma$, i.e. decreasing the angle $\alpha$ (with no analogue for the mass-in-mass chain).

### 2.2 Infinite chain: Dispersion relation

Now consider an infinite chain formed by connecting basic elements with springs $k$, as shown in Fig. 3, and where $k = K = \pi^2\,/\,4$ unless otherwise stated. Assigning superscripts $(n)$ for $n \in \mathbb{Z}$ to the displacements of the masses in the $n$th element along the chain (ordered left to right), the equations of motion for the $n$th element are

$$\left( m + \frac{1}{2} M \left(1 + \gamma^2\right) \right) \frac{\mathrm{d}^2 U_1^{(n)}}{\mathrm{d}t^2} + \frac{1}{2} M \left(1 - \gamma^2\right) \frac{\mathrm{d}^2 U_2^{(n)}}{\mathrm{d}t^2} \tag{11a}$$

$$+ K \left(U_1^{(n)} - U_2^{(n)}\right) + k \left(U_1^{(n)} - U_2^{(n-1)}\right) = 0, \tag{11b}$$

$$\frac{1}{2} M \left(1 - \gamma^2\right) \frac{\mathrm{d}^2 U_1^{(n)}}{\mathrm{d}t^2} + \left( m + \frac{1}{2} M \left(1 + \gamma^2\right) \right) \frac{\mathrm{d}^2 U_2^{(n)}}{\mathrm{d}t^2} \tag{11c}$$

$$+ K \left(U_2^{(n)} - U_1^{(n)}\right) + k \left(U_2^{(n)} - U_1^{(n+1)}\right) = 0. \tag{11d}$$

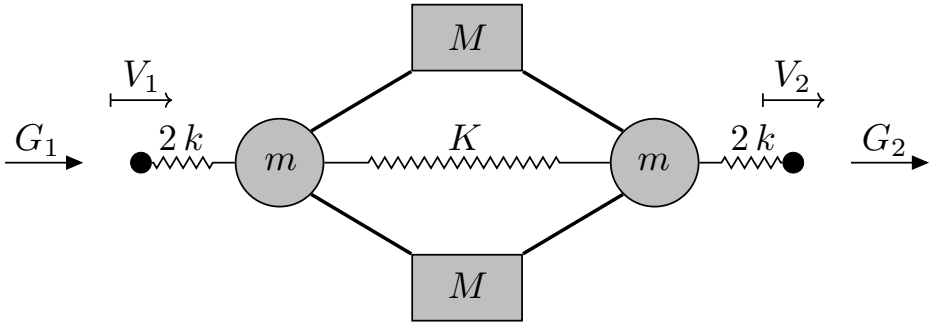


Figure 5: Schematic of unit cell of the chain shown in Fig. 3, with applied forces $G_j(t)$ and resulting displacements $V_j(t)$ of points ($\bullet$) at left- ($j = 1$) and right-hand ($j = 2$) ends of cell.

Fig. 5 shows a unit cell of the infinite chain, in the form of the basic element with half springs attached on either end (thus preserving symmetry). Note that the equivalent spring constant of the series of springs in the unit cell, $k\,K\,/\,(k + K)$, is less than the spring constant of the basic element, $K$. Horizontal forces $G_1(t)$ and $G_2(t)$ are applied to points at the left- and right-hand ends of the cell, respectively, and the resulting horizontal displacements of the points are denoted $V_1(t)$ and $V_2(t)$, respectively. The compliance matrix $\mathbf{D}(\omega)$ for the cell is defined by

$$\begin{pmatrix} v_1 \\ v_2 \end{pmatrix} = \mathbf{D} \begin{pmatrix} g_1 \\ g_2 \end{pmatrix} \quad \text{where } G_j(t) = g_j\,\mathrm{e}^{-\mathrm{i}\,\omega\,t} \text{ and } V_j(t) = v_j\,\mathrm{e}^{-\mathrm{i}\,\omega\,t} \tag{12}$$

for $j = 1, 2$. Following [26], the compliance matrix for the unit cell is calculated from the compliance matrix for the basic element via the relation

$$\mathbf{D}(\omega) = \mathbf{D}_0(\omega) + d_{2\,k}\,\mathbf{I}, \quad \text{where } d_{2\,k} = 1/(2\,k) \tag{13}$$

and $\mathbf{I}$ is the dimension two identity matrix. The stiffness matrix for the unit cell is then simply

$$\mathbf{C} = \begin{pmatrix} c_1 & c_2 \\ c_2 & c_1 \end{pmatrix} \quad \text{where} \quad \mathbf{C}(\omega) = \mathrm{inv}\{\mathbf{D}(\omega)\}. \tag{14}$$

At the anti-resonant frequency of the basic element, $\omega = \omega_*$, the dynamic compliance matrix is a diagonal matrix (and hence so is the stiffness matrix), meaning $\omega_*$ is an anti-resonance for the unit cell. In contrast, the resonant frequency of the basic element, $\omega = \omega_0$, is not a resonant frequency of the unit cell in general, i.e. $\det\{\mathbf{C}(\omega_0)\} \neq 0$.

The compliance matrix (or the stiffness matrix) can be rearranged to calculate the transfer matrix (or monodromy matrix) $\mathbf{P}$, defined via

$$\begin{pmatrix} v_2 \\ g_2 \end{pmatrix} = \mathbf{P} \begin{pmatrix} v_1 \\ -g_1 \end{pmatrix} \quad \text{where} \quad \mathbf{P} = \frac{1}{\hat{d}_2} \begin{pmatrix} \hat{d}_1 + d_{2\,k} & (\hat{d}_1 + d_{2\,k})^2 - \hat{d}_2^2 \\ 1 & \hat{d}_1 + d_{2\,k} \end{pmatrix}. \tag{15}$$

The eigenvalues of the transfer matrix, $\lambda_\pm$, define the Bloch–Floquet wavenumber for the chain, $q$, via $\lambda_\pm = \exp(\pm\mathrm{i}\,q)$, noting that $|\lambda_\pm| = 1$ defines propagating wavenumbers $q \in \mathbb{R}$, i.e. frequencies in the bands, and $|\lambda_\pm| \neq 1$ defines decaying wavenumbers $q \in \mathbb{C}$, i.e. frequencies in bandgaps. The Bloch–Floquet wavenumber satisfies the dispersion relation

$$\mathcal{M}\,\omega_0^{-2}\,\omega^4 + \left\{ \frac{\mathcal{M}\,(1 + 2\,\kappa)}{2\,\kappa} + 2\,\omega_0^{-2} + 2\,\omega_*^{-2}\,\cos q \right\} \omega^2 = 2\,(1 - \cos q), \tag{16}$$

where

$$\mathcal{M} = \frac{2\,(m+M)}{k} \quad \text{and} \quad \kappa = \frac{K}{k} \tag{17}$$

are, respectively, the mass of the basic element and its spring, scaled by the spring connecting the elements.

## 3 Effective monatomic chain

The dispersion relation for the chain can be written compactly in terms of the entries of the compliance matrix $\mathbf{C}$, as

$$c_1 + c_2\,\cos q = 0. \tag{18}$$

Comparing this with the dispersion relation for the effective monatomic chain (shown in Fig. 2), which is

$$m_{\text{eff}}\,\omega^2 = 2\,k\,(1-\cos q), \tag{19}$$

the chain defined by Eqs. (11) corresponds to the effective chain with

$$\frac{m_{\text{eff}}}{k} = \frac{2}{\omega^2}\left(\frac{c_1+c_2}{c_1}\right) \tag{20a}$$

$$= \frac{\mathcal{M}\,\omega_*^2\,\{\omega_0^2 + \kappa\,(\omega_0^2-\omega^2)\}}{\kappa\,\omega_0^2\,(\omega_*^2-\omega^2)}. \tag{20b}$$

The first expression (20a) holds for an arbitrary compliance matrix, whereas the second expression (20b) is specific to the chain defined by Eqs. (11). It can be deduced from Eq. (20b) that the effective mass becomes unboundedly large around the anti-resonant frequency, i.e. as $\omega \to \omega_*$, and hence energy cannot be transferred along the chain. The band edges $q = 0$ and $q = \pi$ can be calculated from Eqs. (19) and (20b), as $\omega = 0$ or $\omega = \omega_-$ for $q = 0$, and $\omega = \omega_0$ or $\omega = \omega_+$ for $q = \pi$, where

$$\omega_- = \omega_0\sqrt{\frac{1+\kappa}{\kappa}} \quad \text{and} \quad \omega_+ = \sqrt{\frac{4}{\mathcal{M}}}, \tag{21}$$

noting that $\omega_+$ is independent of the geometrical parameter $\gamma$.

The left-hand panels of Fig. 6, i.e. (a,c,e), show band diagrams for chains with lightweight attached masses $M = m\,/\,10$, which are an order of magnitude less than the added masses used for the mass-in-mass chains in Fig. 1. The link angle $\alpha$ decreases from top panel to bottom, meaning the geometrical parameter $\gamma$ increases from top to bottom. The band edges $\omega = \omega_0$ and $\omega = \omega_\pm$ are overlaid on the plots, along with the anti-resonant frequency $\omega_*$ (where it exists), and frequency intervals in which $m_{\text{eff}} > 4\,k\,/\,\omega^2$ and $m_{\text{eff}} < 0$ are shaded.

For panel (a), in which the angle $\alpha$ is largest, $\gamma < 1$ meaning the anti-resonant frequency does not exist. Both acoustical and optical branches exist, as for the mass-in-mass chain, but, unlike the mass-in-mass chain, the optical branch is concave down, similar to a diatomic chain [e.g. 27]. A narrow bandgap exists between the acoustical and optical branches, in the interval $2.12 \approx \omega_+ < \omega < \omega_0 \approx 2.20$, for which $m_{\text{eff}} > 4\,k\,/\,\omega^2$. The frequency $\omega = \omega_-$ is the upper edge of the optical branch, and $m_{\text{eff}} < 0$ for frequencies above the optical branch ($\omega > \omega_-$).

For panel (c) the angle is smaller than in panel (a), resulting in smaller values of the band edges $\omega_0$ and $\omega_-$, with $\omega_0 < \omega_+$ so that the bandgap exists in the interval $\omega_0 < \omega < \omega_+$, and thus pushing both the acoustical and optical branches to lower frequencies. Moreover, $\gamma > 1$ meaning the anti-resonant frequency exists, and $\omega_* > \omega_+$ so that the anti-resonant frequency lies above the optical branch. For frequencies immediately above the optical branch $m_{\text{eff}} < 0$, as in panel (a), but for $\omega > \omega_*$ the inequality switches to $m_{\text{eff}} > 4\,k\,/\,\omega^2$. For panel (e), in which the angle is smallest, $\omega_0$ and $\omega_-$ reduce

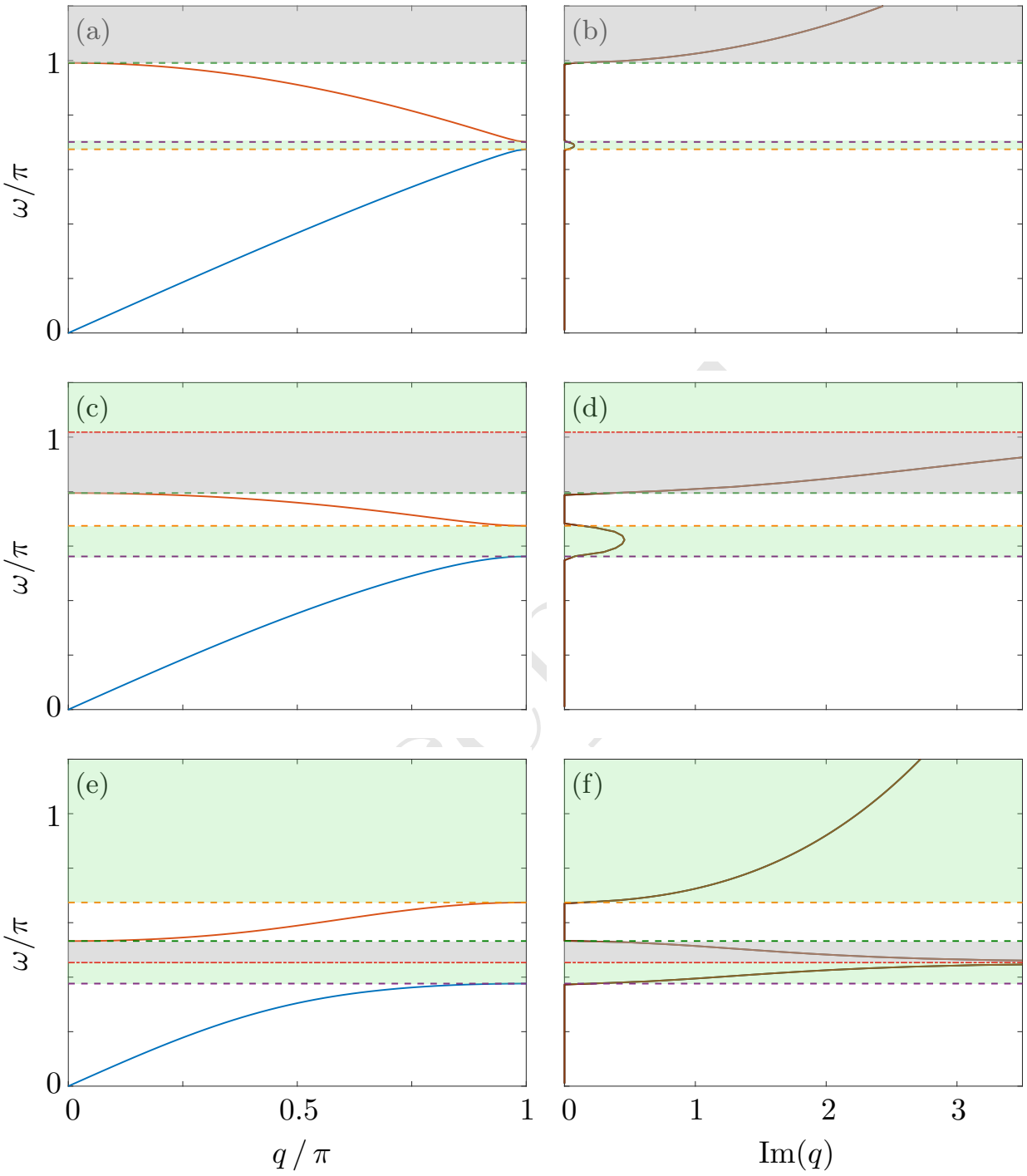


Figure 6: (Left-hand panels, a,c,e) Band diagrams for the chain defined by Eqs. (11) and shown in Fig. 3, with $m = 1$ , $M = 0.1\,m$, and (a) $\alpha = 3\,\pi\,/\,8$, (c) $\alpha = \pi\,/\,8$, (e) $\alpha = \pi\,/\,16$. (Right, b,d,f) Corresponding imaginary values of Bloch–Floquet wavenumber. Frequencies $\omega = \omega_0$ (--), $\omega_-$ (--), $\omega_+$ (--) and $\omega_*$ (-·-) are overlaid, where $\omega_* \in \mathbb{R}$ for (c–f) only. Shaded regions indicate intervals where $m_{\text{eff}} > 4\,k\,/\,\omega^2$ ( ) and $m_{\text{eff}} < 0$ ( ).

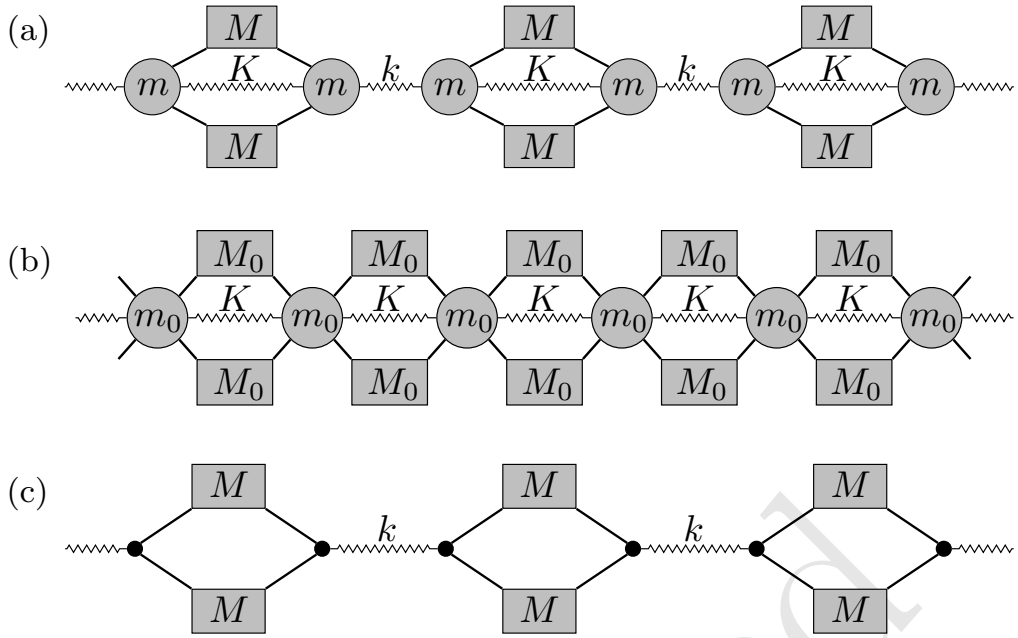


Figure 7: Schematics of (a) proposed chain, (b) Yilmaz et al. chain, and (c) Bobrovnitskii chain.



further, pushing the acoustical and optical branches to even lower frequencies, and causing $\omega_+ < \omega_-$ so that the concavity of the optical branch changes. The anti-resonant frequency also reduces, such that $\omega_* < \omega_-$, meaning the anti-resonant frequency lies in the bandgap, and hence the gap interval below the anti-resonant frequency results from the effective mass satisfying $m_{\text{eff}} > 4\,k\,/\,\omega^2$ and the interval above results from $m_{\text{eff}} < 0$.

The right-hand panels of Fig. 6, i.e. (b,d,f), show the imaginary components of the Bloch–Floquet wavenumber corresponding to the left-hand panels, noting that the imaginary components define attenuation rates along the chain and are only non-zero for frequencies outside the bands, i.e. in the bandgap and above the optical branch. For panel (b), in which the anti-resonant frequency does not exist, the imaginary component is relatively small in the bandgap, with $\text{Im}\,(q) < 0.08$, so that the attenuation is weak. Above the optical branch, the imaginary component grows monotonically with frequency (although, as discussed in § 1, the resulting strong attenuation in the high-frequency regime is not of interest for the present investigation). For panel (d), in which the anti-resonant frequency exists above the optical branch, the imaginary component of the wavenumber in the bandgap attains appreciably greater values than in panel (b), but it remains bounded, with $\text{Im}\,(q) < 0.46$. Immediately above the optical branch, the imaginary component increases rapidly with frequency and becomes unboundedly large as $\omega \to \omega_*$, by definition of the anti-resonant frequency (zero vibrational energy transfer). Above the anti-resonant frequency, the imaginary component initially decreases before increasing monotonically with frequency (not visible, as beyond axes limits). For panel (f), the anti-resonant frequency exists in the bandgap, causing the imaginary component to become unboundedly large within the bandgap, resulting in unboundedly strong attenuation at low frequencies, and thus demonstrating that the geometrical parameter $\gamma$ can be used to generate both low-frequency bandgaps and strong attenuation within the gaps.

# 4 Limiting cases

## 4.1 Yilmaz et al. chain

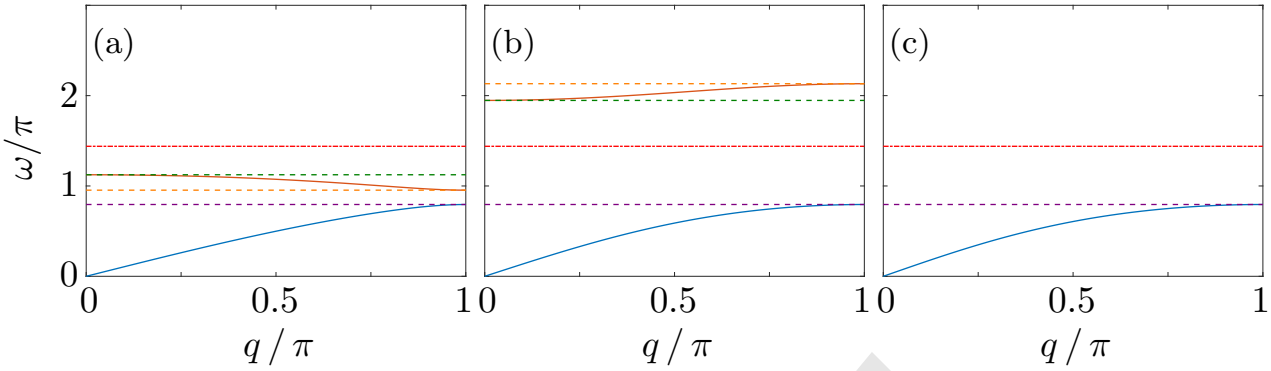


Figure 8: Band diagrams for chain shown in Fig. 7(a), with masses $m = m_0 / 2 = 0.5$ and $M = M_0 = m / 10$, angle $\alpha = \pi / 8$, and springs $K = \pi^2 / 4$, and (a) $k = K$, (b) $k = 5\,K$, (c) $k = 25\,K$, i.e. limiting towards chain shown in Fig. 7(b).

In the limit $k \to \infty$, the chain from §2–3, which is shown in Fig. 7(a), reduces to the Yilmaz et al. chain shown in Fig. 7(b),with masses $M_0 = M$ and $m_0 = 2\,m$. In terms of the new notation, the resonant and anti-resonant frequencies, $\omega_0$ and $\omega_*$, respectively, are

$$\omega_0 = \sqrt{\frac{4\,K}{m_0 + 2\,M_0\,\gamma^2}} \quad \text{and} \quad \omega_* = \sqrt{\frac{2\,K}{M_0\,(\gamma^2 - 1)}}. \tag{22}$$

The band edges $\omega_\pm$ become unboundedly large, i.e. $\omega_\pm \to \infty$, as $k \to \infty$.

Fig. 8 shows band diagrams for attached masses $M_0 = m_0 / 10$, link angles $\alpha = \pi / 8$, and with spring $k$-values increasing from the left panel to right. In all cases, the resonant frequency $\omega_0$ is the upper limit of the acoustical branch, and, as it is independent of the spring $k$, the acoustical branch occupies the same frequency range in panels (a–c). The optical branch occupies a frequency interval bounded by $\omega_\pm$, and, thus, as $k$ increases, the optical branch is pushed to arbitrarily high frequencies (beyond the axes limits in panel c). Therefore, for an operational (bounded) range of frequencies, only the acoustical branch is present in the limit $k \to \infty$.

In the context set out in § 1, of using attached masses to achieve vibration isolation along a monatomic chain with masses $m$ and springs $k$, the masses and springs along the chain shown in Fig. 7(b) are set as $m_0 = m$ and $K = k$. For consistency with the chain shown in Fig. 7(a), the attached mass per mass on the chain is set as $M_0 = M / 2$. Therefore, the resonant and anti-resonant frequencies in Eq. (22) become

$$\omega_0 = \sqrt{\frac{4\,k}{m + M\,\gamma^2}} \quad \text{and} \quad \omega_* = \sqrt{\frac{4\,k}{M\,(\gamma^2 - 1)}}. \tag{23}$$

## 4.2 Bobrovnitskii chain

In the limits $m \to 0$ and $K \to 0$, the chain reduces to the Bobrovnitskii chain, as shown in Fig. 7(c). In the limit $m \to 0$ alone, the resonant frequency becomes

$$\omega_0 = \sqrt{\frac{2\,K}{M\,\gamma^2}} > 0, \tag{24}$$

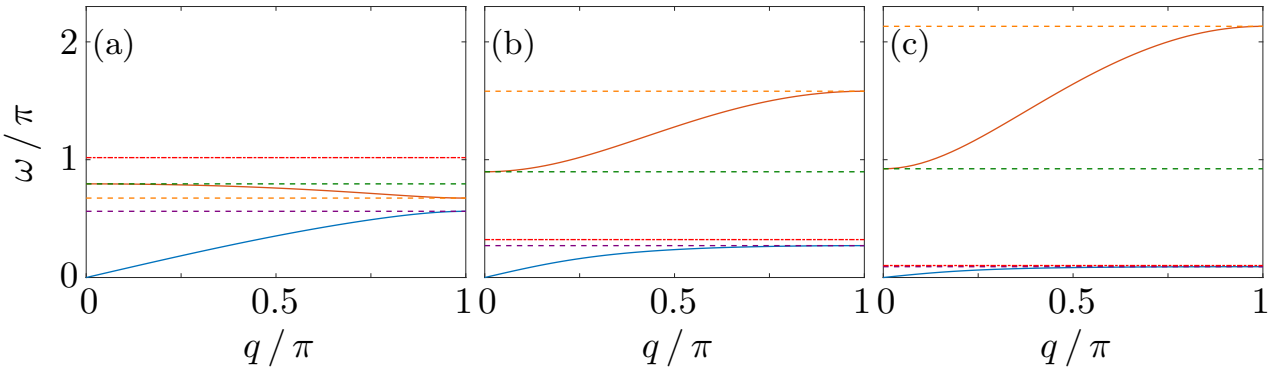


Figure 9: Band diagrams for chain shown in Fig. 7(a), with masses $M = 0.1$, springs $k = \pi^2 / 4$, angle $\alpha = \pi / 8$, and (a) $m = 10\,M$ and $K = k$, (b) $m = M$ and $k = K / 10$, and (c) $m = M / 10$ and $K = k / 100$, i.e. limiting towards chain shown in Fig. 7(c).

and the anti-resonant frequency $\omega_*$ is unchanged from Eq. (10). The band-edge frequencies $\omega_\pm > 0$, so that an acoustical branch exists for arbitrarily small frequencies and the lower limit of the band gap is at a finite frequency. In the limit $K \to 0$ alone, the resonant and anti-resonant frequencies both tend to zero, i.e. $\omega_0$, $\omega_* \to 0$, so that the acoustical branch collapses to $\omega(q) \equiv 0$. The band-edge frequency $\omega_-$ becomes

$$\omega_- = \sqrt{\frac{2\,k}{m + M\,\gamma^2}} > 0, \tag{25}$$

and $\omega_+ > 0$ is unchanged from Eq. (21), so that the lower limit of the optical branch is at a finite frequency above a bandgap that stretches to zero frequency. Therefore, it is the removal of a restoring force in the basic element that causes the zero-frequency bandgap in the Bobrovnitskii chain.

Fig. 9 shows band diagrams for attached masses $M = 0.1$, angles $\alpha = \pi / 8$, and with values of masses $m$ and springs $K$ decreasing from the left panel to right. Again, the resonant frequency $\omega_0$ is the upper bound of the acoustical branch in all cases, and, as it decreases with decreasing $K$, it pushes the acoustical branch onto the $q$-axis. The bounds of the optical branch, $\omega_\pm$, increase with decreasing $m$ and $K$, tending towards the finite (non-zero) limits, with $\omega_- < \omega_+$ in panel (a), swapping to $\omega_- > \omega_+$ in panels (b–c). This causes the optical branch to change concavity, noting that this only occurs only when the anti-resonant frequency exists and concomitantly the anti-resonant frequency moves from above the optical branch into the bandgap.

## 5 Numerical results

Consider a long, finite monatomic chain of length 264, with masses $m = 1$ and springs $k = \pi^2 / 4$. The masses are indexed $n = -129, \ldots, 134$ from left to right. Four lightweight masses $M = m / 8$ are attached to four masses in the middle of the chain, $n = 1, 2, 3, 4$ (giving a net attached mass of $m / 2 = 0.5$), in the form of (i) the mass-in-mass system with attached springs $k$, or (ii) the proposed system involving links, as shown in Figs. 10(a) and (e), respectively. Therefore, the middle of the chain contains either four cells of the mass-in-mass system or two cells of the system with links.

A low-frequency incident wave packet propagates rightwards along the chain, where the wave packet is of toneburst form, and is generated by applying the force $F_{\text{tb}}$ to the leftmost mass $m$ ($n = -129$),

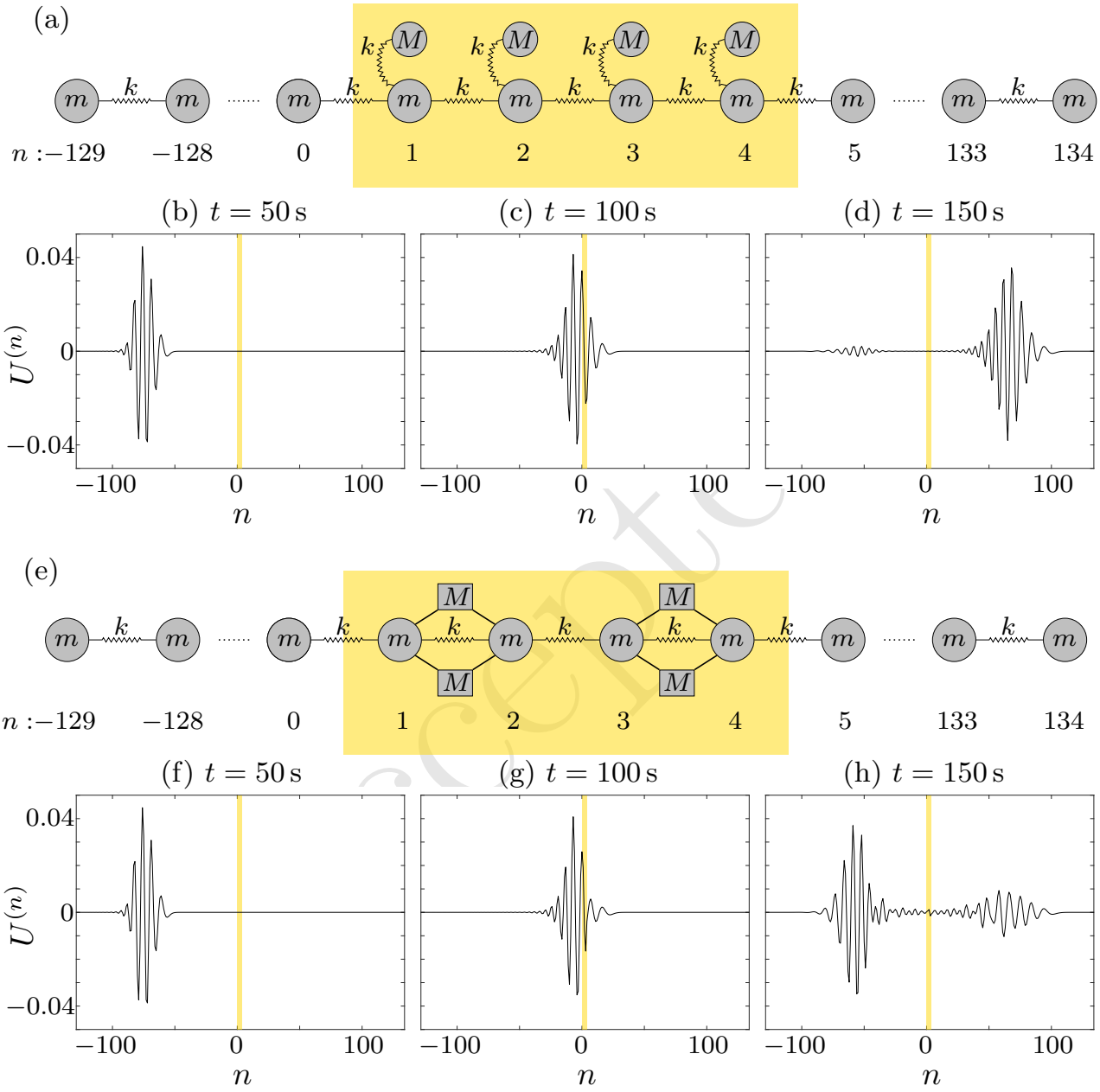


Figure 10: (a,e) Schematics of the long, finite monatomic chain, containing (a) four units cells of the mass-in-mass system, and (e) two unit cells of the system with links. (b–d,f–h) Snapshots of the evolution of the incident wave packet along the chain containing (b–d) the mass-in-mass system, and (f–h) the system involving links, at (left; b,f) $t = 50\,\mathrm{s}$, (middle; c,g) $t = 100\,\mathrm{s}$, and (right; d,h) $t = 150\,\mathrm{s}$. The location of the attached masses are indicated (■).

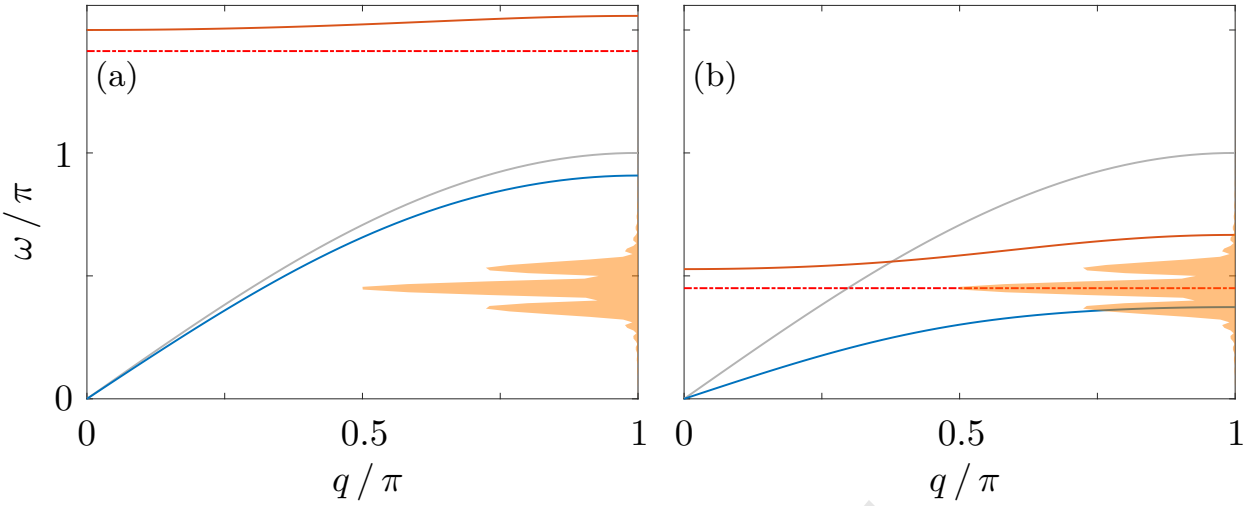


Figure 11: Band diagrams for (a) the mass-in-mass system and (b) the system with links, with $m = 1$, $M = m/8$ and $\omega_{\rm ct} = 0.45\,\pi$, and including the anti-resonant frequencies. The dispersion curve for the monatomic chain (—), and the Fourier transform of the toneburst forcing $\mathcal{F}(F_{\rm tb})$ (■) are overlaid, where $\max\{\mathcal{F}(F_{\rm tb})\} \approx 0.006$.

where

$$F_{\rm tb}(t) = \begin{cases} \dfrac{a}{2}\left(1 - \cos\left(\dfrac{\omega_{\rm ct}\,t}{N_{\rm cy}}\right)\right)\cos(\omega_{\rm ct}\,t) & \text{for} \quad t < \dfrac{2\,\pi\,N_{\rm cy}}{\omega_{\rm ct}} \\ 0 & \text{otherwise,} \end{cases} \tag{26}$$

in which $a = 0.1\,\mathrm{N}$ is the force amplitude, $\omega_{\rm ct}$ is the central packet frequency and $N_{\rm cy} = 5$ is the number of packet cycles. The attached masses are arranged to minimise transmission of the wave packet into the right-hand side of the chain. For the mass-in-mass system, this simply means attaching the full mass available. For the system involving links, the angle of the links is chosen so that the anti-resonant frequency coincides with the central frequency, i.e.

$$\alpha = \hat{\alpha}(\omega_{\rm ct}) \equiv \operatorname{arccot}\left(\sqrt{1 + \frac{2\,k}{M\,\omega_{\rm ct}^2}}\right). \tag{27}$$

Fig. 11 shows the band diagrams for the two systems (including the anti-resonant frequencies), with the dispersion curve for the underlying monatomic chain (of the acoustical type) and the Fourier transform of the toneburst forcing $\mathcal{F}(F_{\rm tb})$ both overlaid, where the central wave frequency is $\omega_{\rm ct} = 0.45\,\pi$. For the lightweight attached masses used, the bandgap of the mass-in-mass system occupies the relatively high-frequency interval $0.91\,\pi < \omega < 1.5\,\pi$, with the anti-resonant frequency $\omega_* \approx 1.4\,\pi$ close to the top of the gap. The most strongly excited frequencies of the incident packet, say $\mathcal{F}(F_{\rm tb}) > \max\{\mathcal{F}(F_{\rm tb})\}/6$, are $0.33\,\pi < \omega < 0.57\,\pi$, and lie approximately in the middle of the frequency interval occupied by the acoustical branch, where the acoustical branch is close to that of the monatomic chain. For the system with links, setting the angle according to Eq. (27), $\alpha = \hat{\alpha}(0.45\,\pi) \approx 0.069\,\pi \approx 12.42°$, means that the anti-resonant frequency $\omega_* = \omega_{\rm ct}$, so that the bandgap interval $0.37\,\pi < \omega < 0.53\,\pi$ is roughly centred around the central frequency of the incident packet, and only the fringes of the most strongly generated incident frequencies are on the dispersion curves.

Figs. 10(b–d) and (f–h) show snapshots of the evolution of the (longitudinal) incident wave packet along the chain, for the chain containing (b–d) the mass-in-mass system, and (f–h) the link system. The left-hand panels (b,f) show the incident packet prior to interaction with the interval containing the

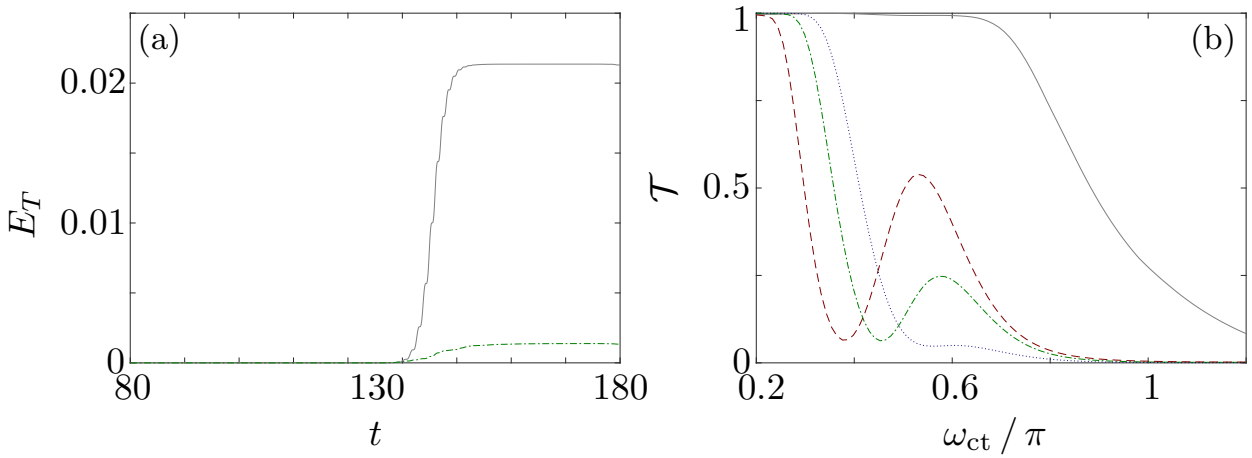


Figure 12: (a) Evolution of the transmitted energy for the tests shown in Fig. 10 (chain containing mass-in-mass system —, and system involving links ···). (b) Transmission coefficient as a function of central incident frequency, for chain containing mass-in-mass system (—), and system involving links with $\alpha = \hat{\alpha}(0.55\,\pi)$ (—), $\hat{\alpha}(0.45\,\pi)$ (···), and $\hat{\alpha}(0.35\,\pi)$ (– –).

attached masses (shaded gold region), and the middle panels (c,g) show the packet during interaction with the attached masses. The right-hand panels (d,h) show the packet following the interaction, in which the packet is split into a reflected component (on the left) and a transmitted component (on the right). For the chain containing the mass-in-mass system, the majority of the incident packet is transmitted, with only a small reflected component, as the packet lies on the acoustical branch in an interval where the acoustical branch is close to that of the monatomic chain, so that the mass-in-mass system is nearly impedance matched with the surrounding monatomic chain. For the chain containing the link system, the majority of the incident packet is reflected, as the packet frequencies are strongly attenuated by the link system.

Fig. 12(a) quantifies the transmissions shown in Fig. 10, in terms of the evolution of the transmitted energies $E_T(t)$, which are calculated as the sum of kinetic and potential energies of the masses on the right-hand side of the interval containing the attached masses. The energies are zero up to $t \approx 100\,\mathrm{s}$, when the first components of the incident wave packet reach the masses on the right, after which the energies increase monotonically until they plateau at steady, maximum values. The maximum transmitted energy for the chain containing the mass-in-mass system (—) is $\approx 16$ times greater than the maximum for the chain containing the link system (···).

Fig. 12(b) shows transmission coefficients, $\mathcal{T}$, as functions of the central incident frequency, $\omega_{\mathrm{ct}}$, where the transmission coefficient is defined as the steady, maximum transmitted energy normalised by the maximum incident energy, i.e. $\mathcal{T} = \max(E_T) \,/\, \max(E_I)$. For the chain containing the mass-in-mass system (—), the incident energy is fully transmitted, i.e. $\mathcal{T} \approx 1$, for $\omega_{\mathrm{ct}} \leq 0.6\,\pi$. As the central frequency increases above this threshold, the transmission coefficient reduces monotonically, reaching $\mathcal{T} \approx 0.09$ for the highest frequency considered, $\omega_{\mathrm{ct}} = 1.2\,\pi$, recalling that the anti-resonant frequency for the mass-in-mass system, $\omega_* \approx 1.4\,\pi$, lies just above the frequency range shown. For the chain containing the link system (···), transmission is full for only the lowest frequencies considered, $\omega_{\mathrm{ct}} \leq 0.25\,\pi$. As the central frequency increases above $\omega_{\mathrm{ct}} = 0.25\,\pi$, the transmission coefficient decreases rapidly, reaching a local minimum of $\mathcal{T} \approx 0.06$ at $\omega_{\mathrm{ct}} = \omega_* = 0.45\,\pi$, then increasing to a local maximum of $\mathcal{T} \approx 0.25$ at $\omega_{\mathrm{ct}} \approx 0.57\,\pi$, close to the upper bound of the bandgap, and then monotonically decreasing to zero at $\omega_{\mathrm{ct}} \approx 1$. Transmission coefficients are also shown for the chain containing the link system with angles $\alpha = \hat{\alpha}(0.35\,\pi) \approx 0.054\,\pi$ (– –) and $\alpha = \hat{\alpha}(0.55\,\pi) \approx 0.083\,\pi$ (—). The qualitative behaviour of the transmission coefficient as a function of $\omega_{\mathrm{ct}}$ is unchanged by the

variations in angle, but the low-frequency local extrema shift to lower/higher frequencies as the angle is decreased/increased, with the locations of the local minima dictated by the anti-resonant frequencies. Further, the local minimum value increases/decreases slightly as the angle is decreased/increased, and the local maximum strongly increases/decreases as the angle is decreased/increased, so that it is barely visible for the largest angle considered, $\alpha \approx 0.083\,\pi$.

# 6 Conclusions

An acoustical metamaterial chain has been proposed for efficient low-frequency vibration isolation. The chain consists of a modified monatomic chain plus a system of lightweight masses attached to the chain with rigid links, in which the mean link angle acts as a tunable geometrical parameter. The vibration-isolation properties of the proposed system were determined from the resonant and anti-resonant frequencies of a basic chain element, using an efficient relation between the dynamic compliance and stiffness matrices of the basic element and a unit cell of the chain. The compliance/stiffness matrix formulation facilitated straightforward derivation of the effective mass of the chain, and the derived expression identified the roles of the resonant and anti-resonant frequencies in the effective mass. It was shown that decreasing the link angle lowers the resonant and anti-resonant frequencies (with the anti-resonant frequency existing only below a certain link angle), thus forcing the bandgap to lower frequencies, and the anti-resonant frequency into the bandgap, so that efficient low-frequency vibration isolation is achieved by tuning the geometry rather than the mass of the attached system.

The proposed metamaterial chain was shown to generalise two existing chains with similar tunable geometrical parameters (attributed to Yilmaz et al. and Bobrovnitskii, respectively), and these chains were obtained by taking certain parameter limits of the proposed chain. The single dispersion curve of the Yilmaz et al. chain was shown to have similar properties to the acoustical branch of the proposed chain. Taking the Bobrovnitskii limit was shown to force the acoustical branch of the proposed chain, and hence the bandgap, to arbitrarily low frequencies, but only at the potentially impractical cost of losing the restoring force between masses in a basic element.

A numerical test was conducted to illustrate the low-frequency vibration-isolation properties of the proposed system, in which a prescribed net attached mass was attached in the middle of a long monatomic chain in the form of two units of the system. The link angle in the system was chosen to minimise transmission of a wave packet generated at one end of the chain, by setting the anti-resonant frequency equal to the central wave packet frequency. This approach was shown to reduce the transmitted energy by an order of magnitude, in comparison to applying same net attached mass in the form of four units of the standard mass-in-mass system. Further, the energy transmitted through the system was shown to remain small when the central wave frequency was varied, without the need to re-tune the link angle/anti-resonant frequency.



# References

[1] B. Voigtländer, P. Coenen, V. Cherepanov, P. Borgens, T. Duden, and F. S. Tautz. Low vibration laboratory with a single-stage vibration isolation for microscopy applications. *Rev. Sci. Inst.*, 88 (2):1–8, 2017.

[2] T. Bein, J. Bös, S. Herold, D. Mayer, T. Melz, and M. Thomaier. Smart interfaces and semi-active vibration absorber for noise reduction in vehicle structures. *Aero. Sci. Technol.*, 12(1): 62–73, 2008.

[3] W. Johnson and M. Ruzzene. Challenges and constraints in the application of resonance-based metamaterials for vibration isolation. *Proc SPIE, 10600, Health Monitoring of Structural and Biological Systems XII*, page 1060024, 2018.

[4] P. G. Dylejko, I. R. MacGillivray, S. M. Moore, and A. Skvortsov. The Influence of Internal Resonances From Machinery Mounts on Radiated Noise From Ships. *IEEE J. Ocean. Eng.*, 42 (2):399–409, 2017.

[5] Guancong Ma and Ping Sheng. Acoustic metamaterials: From local resonances to broad horizons. *Sci. Adv.*, 2:e1501595, 2016. ISSN 2375-2548.

[6] Shuang Chen, Yuancheng Fan, Quanhong Fu, Hongjing Wu, Yabin Jin, Jianbang Zheng, and Fuli Zhang. A review of tunable acoustic metamaterials. *Appl. Sci.*, 8(9):1480, 2018.

[7] Richard V. Craster and Sbastien Guenneau, editors. *Acoustic metamaterials: negative refraction, imaging, lensing and cloaking.* Number 166 in Springer series in materials science. Springer, Dordrecht ; New York, 2013. ISBN 978-94-007-4812-5.

[8] Penglin Gao, Alfonso Climente, Jos Snchez-Dehesa, and Linzhi Wu. Single-phase metamaterial plates for broadband vibration suppression at low frequencies. *J. Sound Vib.*, 444:108–126, 2019.

[9] Hao-Jiang Zhao, Hong-Wei Guo, Bing-Yan Li, Zong-Quan Deng, and Rong-Qiang Liu. Flexural vibration band gaps in a double-side phononic crystal plate. *J. Appl. Phys.*, 118:044906, 2015.

[10] Hao-Jiang Zhao, Hong-Wei Guo, Ming-Xing Gao, Rong-Qiang Liu, and Zong-Quan Deng. Vibration band gaps in double-vibrator pillared phononic crystal plate. *J. Appl. Phys.*, 119(1):014903, 2016.

[11] Etienne Coffy, Thomas Lavergne, Mahmoud Addouche, Sbastien Euphrasie, Pascal Vairac, and Abdelkrim Khelif. Ultra-wide acoustic band gaps in pillar-based phononic crystal strips. *J. Appl. Phys.*, 118:214902, 2015.

[12] Osama R. Bilal, Andr Foehr, and Chiara Daraio. Observation of trampoline phenomena in 3d-printed metamaterial plates. *Extreme Mech. Lett.*, 15:103–107, 2017.

[13] Osama R. Bilal, David Ballagi, and Chiara Daraio. Architected lattices for simultaneous broadband attenuation of airborne sound and mechanical vibrations in all directions. *Phys. Rev. Appl.*, 10:054060, 2018.

[14] H. H. Huang, C T Sun, and G. L. Huang. On the negative effective mass density in acoustic metamaterials. *Int. J. Eng. Sci.*, 47(4):610–617, 2009.

[15] G. L. Huang and C. T. Sun. Band gaps in a multiresonator acoustic metamaterial. *J. Vib. Acoust.*, 132(3):031003, 2010.

[16] B. S. Lazarov and J. S. Jensen. Low-frequency band gaps in chains with attached non-linear oscillators. *Int. J. Non-Lin. Mech.*, 42(10):1186–1193, 2007.

[17] C. Yilmaz, G. M. Hulbert, and N. Kikuchi. Phononic band gaps induced by inertial amplification in periodic media. *Phys. Rev. B*, 76:054309, 2007.

[18] C. Yilmaz and G. M. Hulbert. Theory of phononic gaps induced by inertial amplification in finite structures. *Phys. Lett. A*, 374(34):3576–3584, 2010. ISSN 03759601.

[19] G. Acar and C. Yilmaz. Experimental and numerical evidence for the existence of wide and deep phononic gaps induced by inertial amplification in two-dimensional solid structures. *J. Sound Vib.*, 332(24):6389–6404, 2013.

[20] H. H. Huang and C. T. Sun. Theoretical investigation of the behavior of an acoustic metamaterial with extreme Youngs modulus. *J. Mech. Phys. Solids*, 59(10):2070–2081, 2011. ISSN 00225096.

[21] N. M. M. Frandsen, O. R. Bilal, J. S. Jensen, and M. I. Hussein. Inertial amplification of continuous structures: Large band gaps from small masses. *J. Appl. Phys.*, 119:124902, 2016.

[22] Y. I. Bobrovnitskii. An acoustic metamaterial with unusual wave properties. *Acoust. Phys.*, 60 (4):371–378, 2014. ISSN 1063-7710.

[23] Joo Hwan Oh, Seong Jae Choi, Jun Kyu Lee, and Yoon Young Kim. Zero-frequency Bragg gap by spin-harnessed metamaterial. *New J. Phys.*, 20:083035, 2018.

[24] J. H. Oh and B. Assouar. Quasi-static stop band with flexural metamaterial having zero rotational stiffness. *Sci. Rep.*, 6:33410–33410, 2016.

[25] Andr Foehr, Osama R. Bilal, Sebastian D. Huber, and Chiara Daraio. Spiral-based phononic plates: From wave beaming to topological insulators. *Phys. Rev. Lett.*, 120(20):205501, 2018.

[26] Y. I. Bobrovnitskii. Models and general wave properties of two-dimensional acoustic metamaterials and media. *Acoust. Phys.*, 60(2):134–141, 2014. ISSN 1063-7710.

[27] N. M. M. Frandsen and J. S. Jensen. Modal interaction and higher harmonic generation in a weakly nonlinear, periodic mass-spring chain. *Wave Motion*, 68:149–161, 2017.